AGU PUBLICATIONS

JGR

Journal of Geophysical Research: Oceans

RESEARCH ARTICLE

10.1002/2016JC012496

Key Points:
- Unique field data set on joint landslide deposit and tsunami runup presented
- First model to show that frequency dispersion is needed to closely reproduce runup field data
- Optimization procedure used to retrofit the likely landslide dynamics

Correspondence to:
S. S. Gylfadóttir,
siggasif@vedur.is

Citation:
Gylfadóttir, S. S., J. Kim, J. K. Helgason, S. Brynjólfsson, Á. Höskuldsson, T. Jóhannesson, C. B. Harbitz, and F. Løvholt (2017), The 2014 Lake Askja rockslide-induced tsunami: Optimization of numerical tsunami model using observed data, *J. Geophys. Res. Oceans*, *122*, 4110–4122, doi:10.1002/2016JC012496.

Received 21 OCT 2016
Accepted 20 MAR 2017
Accepted article online 23 MAR 2017
Published online 18 MAY 2017

The 2014 Lake Askja rockslide-induced tsunami: Optimization of numerical tsunami model using observed data

Sigríður Sif Gylfadóttir[1], Jihwan Kim[2], Jón Kristinn Helgason[1], Sveinn Brynjólfsson[1], Ármann Höskuldsson[3], Tómas Jóhannesson[1], Carl Bonnevie Harbitz[2], and Finn Løvholt[2]

[1]Icelandic Meteorological Office, Reykjavík, Iceland, [2]Norwegian Geotechnical Institute, Oslo, Norway, [3]Institute of Earth Sciences, University of Iceland, Reykjavík, Iceland

Abstract A large rockslide was released from the inner Askja caldera into Lake Askja, Iceland, on 21 July 2014. Upon entering the lake, it caused a large tsunami that traveled about ~3 km across the lake and inundated the shore with vertical runup measuring up to 60–80 m. Following the event, comprehensive field data were collected, including GPS measurements of the inundation and multibeam echo soundings of the lake bathymetry. Using this exhaustive data set, numerical modeling of the tsunami has been conducted using both a nonlinear shallow water model and a Boussinesq-type model that includes frequency dispersion. To constrain unknown landslide parameters, a global optimization algorithm, Differential Evolution, was employed, resulting in a parameter set that minimized the deviation from measured inundation. The tsunami model of Lake Askja is the first example where we have been able to utilize field data to show that frequency dispersion is needed to explain the tsunami wave radiation pattern and that shallow water theory falls short. We were able to fit the trend in tsunami runup observations around the entire lake using the Boussinesq model. In contrast, the shallow water model gave a different runup pattern and produced pronounced offsets in certain areas. The well-documented Lake Askja tsunami thus provided a unique opportunity to explore and capture the essential physics of landslide tsunami generation and propagation through numerical modeling. Moreover, the study of the event is important because this dispersive nature is likely to occur for other subaerial impact tsunamis.

1. Introduction

The Askja central volcano is located in the Northern Volcanic Zone of Iceland. The main caldera was formed in an eruption at the end of the last Ice Age 10,000 years ago. An explosive eruption in March 1875 led to the formation of an inner caldera, which over the next 40 years gradually subsided and filled up with water to form Lake Askja [*Hartley and Thordarson*, 2012]. The lake covers an area of 11 km^2 and has a maximum depth of approximately 220 m, a typical depth between 150 and 200 m at the center of the basin and an average depth of 114 m. To the south and east, it is bounded by steep talus slopes rising over 350 m above the lake water level while the northern and western sides are defined by 60 m high cliffs. The 60 m deep Víti explosion crater formed during the 1875 eruption on the northeast shore of the lake. A map of Askja is shown in Figure 1. A large rock avalanche was released from the southeast margin into Lake Askja on 21 July 2014. The release zone was located from 150 to 370 m above the water level and the main scarp measured 800 m long. The volume of the rockslide deposit is estimated to be 20×10^6 m^3, of which 10×10^6 m^3 was deposited in the lake and caused the water level to be raised by over half a meter. Upon entering the lake, the rockslide had a width of approximately 550 m and caused a sizable tsunami that traveled across the lake in 1–2 min (based on numerical modeling) and inundated the shores around the entire lake. The vertical runup varied considerably depending on the alongshore position but measured several tens of meters in many places. Lake Askja is a popular tourist destination and is visited by tens of thousands of tourists every year. During the peak of summer, it can be expected that over a day between 100 and 200 people visit Askja. As luck would have it, the event occurred near midnight when no one was in the area.

A similar event occurred in British Columbia, Canada, in December 2007 when a 3×10^6 m^3 landslide entered Chehalis Lake, a popular tourist destination, and generated a tsunami that inundated the shoreline up to 38 m above the lake level [*Roberts et al.*, 2013; *Lawrence et al.*, 2013; *Wang et al.*, 2015]. Had the event

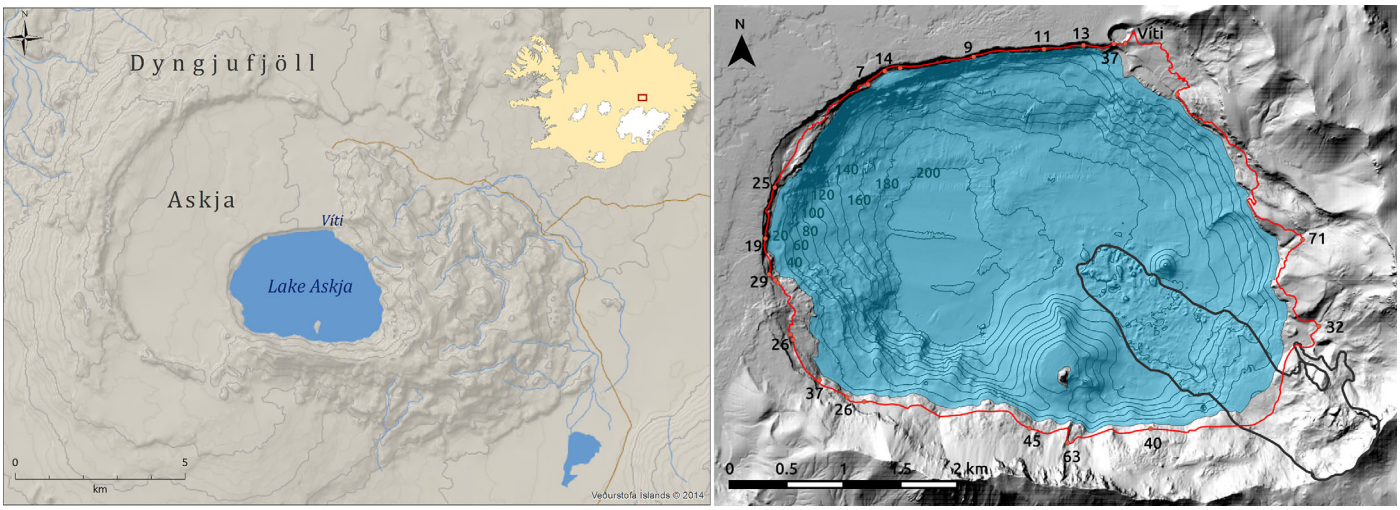

Figure 1. (left) The Askja caldera. (right) Overview of Lake Askja after the rockslide. The hillshade is based on bathymetric data gathered through a Multibeam survey conducted by the University of Iceland, and topographic data from an aerial survey by the Ludwig-Maximilians-Universität München (courtesy of the IsViews project, www.isviews.geo.lmu.de). The thick dark line marks the outline of the rockslide. Measured inundation is shown with a red line and numbers indicate the measured inundation heights at selected points.

not occurred during off-season, it would almost certainly have resulted in injuries and loss of lives as the lake is surrounded by numerous campsites. There are many other well-documented events in the last century that bear witness to the great destructive power of rockslide-induced tsunamis. The largest known subaerial landslide-induced tsunami occurred in Lituya Bay, Alaska in 1958, with a maximum inundation of 524 m above sea level [*Fritz et al*., 2009; *Miller*, 1960; *Mader and Gittings*, 2002; *Weiss et al*., 2009]. Not long after that, in 1963, a gigantic rockslide into the Vajont reservoir in northern Italy generated a 250 m high wave that overtopped the dam. The flood wave travelled downvalley completely destroying several villages and killing almost 2000 people [*Ghirotti*, 2012; *Kiersch*, 1964; *Müller*, 1964, 1968]. In Norway, narrow fjords bounded by steep mountains create an environment of significant tsunami hazard which has led to some of the largest natural disasters in the country's history. During the last century, the 1934 Tafjord as well as the 1905 and 1936 Loen events devastated several villages along the shores of Storfjorden and Lake Loen and caused the loss of 174 lives [*Harbitz et al*., 1993, 2014; *Furseth*, 1985, 2009; *Jørstad*, 1968]. In 1971, a 100,000 m^3 rock avalanche plunged into Yanahuin Lake in Chungar, Peru, creating a tsunami that washed up to 30 m elevation above the lake level. Several hundred people were killed and most of the surface facilities of the Chungar mine demolished [*Plafker and Eyzaguirre*, 1979]. More recently, in 2007, 10 people were killed after an earthquake triggered hundreds of subaerial landslides along the shores of the Aysén fjord (Chilean Patagonia), of which several entered the fjord and generated a series of tsunamis with a maximum runup of several tens of meters [*Naranjo et al*., 2009; *Sepúlveda et al*., 2010; *Hermanns et al*., 2014]. *Freundt et al*. [2007] give several additional examples of devastating lake tsunami events triggered by volcanic activity or instability of volcanic formations.

Extensive measurements of the Lake Askja rockslide deposits and its visible consequences have been conducted by the Icelandic Meteorological Office (IMO), the Institute of Earth Sciences (IES) of the University of Iceland (UI), the Institute of Geography at the University of Innsbruck (UIBK), and the Ludwig-Maximilians-Universität München (LMU). Shortly after the event, signs of the tsunami inundation around the lake were surveyed with GPS and laser equipment and the change in water level was measured. A high-resolution digital elevation model (DEM) of the entire Lake Askja caldera was created from aerial photographs by stereo photogrammetry based on an airborne survey conducted by the LMU team. High-resolution bathymetric data were obtained through a multibeam sonar sounding survey by the IES and the IMO. In addition, aerial photographs of the release area and surroundings were taken by Loftmyndir Ltd. in 2013 and 2014 and DEMs of 5 m resolution before and after the slide have been compiled on the basis of those. Earthquakes associated with the event have been analyzed and seismic modeling will be carried out to extract information about the release mechanism and dynamics of the slide. Lastly, numerous photographs of the slide area from before and after the event have been collected in addition to photographs of the release area and runup area of the tsunami that were taken from an unmanned aerial vehicle shortly after the event.

Figure 1 shows a hillshade map of the combined bathymetry and topography of Lake Askja in addition to the measured inundation around the lake.

Numerical tsunami models typically employ the shallow water approximation, whereby the Navier-Stokes equations are reduced to two dimensions by assuming that the wavelength of the generated waves is very long compared to the depth of the water. In the case of earthquake-triggered tsunamis, this is often an appropriate assumption but it is most often not valid for landslide-induced tsunamis as shorter waves are generated due to the landslide impact [*Glimsdal et al*., 2013; *Løvholt et al*., 2015a]. In the shallow water approximation, the phase velocity is independent of wavelength. In reality, however, frequency dispersion leads to a spreading of the wave train. In this case, depth-averaged equations of the Boussinesq type become more appropriate to describe the wave generation and propagation.

The Lake Askja tsunami provides a unique opportunity to explore and capture the essential physics of landslide tsunami generation and propagation through numerical modeling, given the exhaustive amount of data to calibrate the model. The comprehensive documentation of the event in combination with the use of a new Boussinesq-type model is rather unique. Making optimal use of the comparison between field observations and runup simulations enabled us to delineate the physics of impact tsunamis without the scale effects that are present in the laboratory.

The focus of the work presented here is manifold. First, to present the comprehensive field data including landslide deposits and tsunami runup data. Second, to apply an optimization procedure to determine unknown landslide parameters through comparison between measured and calculated inundation in an inverse modeling approach. Third, to explore the importance of dispersion by comparing results from a nonlinear shallow water (NLSW) model developed in GeoClaw [*Berger et al*., 2011] with results from an extension to GeoClaw that includes dispersion, labeled BoussClaw [*Kim*, 2014; *Kim et al*., 2017].

The paper is organized as follows: a description of the event and the data used for modeling is presented in section 2. The numerical model is discussed in section 3, beginning with the block model of the landslide (section 3.1). After that, the two numerical methods for modeling the tsunami are described, the NLSW model developed in GeoClaw (section 3.2.1) and the Boussinesq-type extension to GeoClaw that includes dispersion (section 3.2.2). The model setup is discussed in section 3.3. Finally, the modeling results are presented in section 4 and conclusions in section 5.

2. The Lake Askja Rockslide and Tsunami

2.1. The Event

The Askja landslide was released on the evening of 21 July 2014 from the southeast caldera wall. The landslide is one of the largest known rockslides since the settlement of Iceland in the ninth century A.D. It was registered as tremor at IMO seismic stations near Askja and the data show that the event occurred at 23:24 local time. A signal was also detected by an infrasound array in the south of Iceland, at a distance of roughly 210 km. No one was in the area but a group located about 16 km ENE of the site witnessed a large plume of smoke or vapor spreading rapidly and ascending up to the cloud cover.

The failure occurred along a known ring fault that is associated with the subsidence of the caldera [*Hartley and Thordarson*, 2012]. Photographic evidence suggests that creeping in the source area started in 2007 and the vertical displacement between August 2007 and the 21 of July 2014 is estimated to have been at least 25 m. Analysis of photographs shows that accelerating deformation of the landslide source area was visible weeks prior to the event, as tension cracks within the mass and in the snow that covered part of the mountainside. The photographs also indicated that the head crown of the landslide had started to form.

The landslide left behind a crescent shaped scarp within the caldera wall typical of a rotational blockslide. Part of the material was left behind as Toreva-like slump blocks while part of it slid down into Lake Askja. The depth of the failure plane is uncertain, making it difficult to determine the total volume of material set in motion but it is estimated to have been about 20×10^6 m^3 based on field data (see section 2.2.2).

Several factors contributed to the release of the slide. Movements on an active ring fault and changes in crustal stress induced by long-term subsidence at the center of the Askja caldera due to pressure changes

Figure 2. (left) The signs of the tsunami were clearly visible as black sand deposited on snow patches surrounding the lake. (right) The rise in water level was estimated by comparing photographs from before and after the event. Photos: Sveinn Brynjólfsson.

in the magma chamber below have led to an increased instability in the southeast rim of the caldera [*Sigmundsson et al.*, 2014]. However, the main factors believed to have triggered the release are geothermal alteration and associated weakening of the bedrock along with snowmelt and heavy precipitation in the days prior to the event.

Bathymetric data suggest that the sliding block had not undergone extensive disintegration when it entered the lake, but that the degradation occurred during underwater movement. The landslide traveled close to 2 km along the bottom of the lake and caused a large tsunami that travelled across the lake inundating the shoreline up to an elevation of 60–80 m in places. The tsunami left behind clear evidence of the inundation. Snow patches around the lake were blackened by deposition of sediments and severe erosion was visible at several locations. The morning following the event, seiches on the lake were evident from the sound of pumice rolling against the beach.

2.2. Data

2.2.1. Maximum Inundation

Figure 1 shows the measured inundation on a hillshade of an elevation model of the area after the landslide. The maximum inundation was measured by tracing the sediment deposits on snow patches around the lake. These are shown in a photograph in Figure 2. In places that were easily accessible, the inundation lines were traced with GPS measurements. Elsewhere, Leica VECTOR rangefinder binoculars were used to pinpoint inundation traces. In addition, signs of erosion or sediment deposition from high-resolution aerial photographs were used to fill in the gaps.

2.2.2. Lake Water Level and Submerged Rockslide Volume

The rockslide deposited a 2.1 km long and on average 600 m wide tongue on the bottom of the lake resulting in a rise of the lake water level. To quantify the magnitude of the change in water level, photographs showing selected rocks and cliffs at the lake level from shortly before and 2 weeks after the event were obtained. From the photographs, notable features such as fractures were identified and their position above the preslide and postslide water level measured, as shown in Figure 2. Using accurate GPS measurements of the water level to estimate the change over the time period from shortly after the event to the time of the latter set of photographs, the change in water level caused by the landslide was estimated as 0.65 ± 0.2 m. As the lake has an area of 11.7 km^2 this corresponds to a submerged landslide volume of $7.5 \pm 2 \times 10^6$ m^3 or approximately $10 \pm 3 \times 10^6$ m^3 of landslide debris on dry land with 30% porosity. Since the moving submerged landslide will contain a substantial amount of entrained air over the short time of propagation on the lake bottom, we opt to use the latter value of 10×10^6 m^3 in model computations of the waves induced by the landslide.

2.2.3. Bathymetry Before and After the Landslide

Low-resolution single beam soundings of Lake Askja were carried out in 1963 [*Rist*, 1975]. High-resolution bathymetry data for Lake Askja were first compiled from multibeam echo soundings in 2012 and the results used to construct a bathymetric map with 2 m horizontal resolution [*Fridriksson*, 2014]. Weather conditions deteriorated during the survey, which had to be aborted before it was completed, leaving an area in the southeastern part of the lake uncovered. This is precisely the region where the landslide entered the lake.

Shortly after the landslide in 2014, a second multibeam survey was conducted by the IES. The interpretation of the data resulted in an extremely detailed bathymetry model showing clearly the landslide deposit on the lake bottom (Figure 1). This data set forms the basis of the bathymetry model used in the numerical modeling of the tsunami. The regions with rockslide deposits were filled in with data from 2012 where possible. The average thickness of the deposits as revealed by the multibeam survey is roughly 8 m. In the southeast part where no data are available, the deposits were removed from the DEM by moving elevation contours back by up to 10–15 m and interpolating the results onto a grid. The topography around the lake was then stitched to the bathymetry model using a digital elevation model based on aerial photographs from 2013. The final resolution of the terrain model used for the numerical modeling is 5 × 5 m.

3. Numerical Model

3.1. Block Velocity Model

The primary purpose of the present investigation was to use the tsunami observations in combination with numerical tsunami models to provide first order understanding of the landslide speed, tsunami propagation and inundation pattern. Given the various uncertainties in question, a simple block model approach was used to describe the motion of the rockslide. At time $t = 0$, the block enters the lake with initial velocity U_0 and travels along the lake bottom influenced by gravity, buoyancy, bed friction, and pressure drag. The motion of the rockslide center of mass (CM) in the lake is described by

$$(m_l+\delta m_l)\frac{dU}{dt}=(m_l-\rho_w V_w)g(\sin\phi-\mu\cos\phi) -\frac{1}{2}\rho_w C_d A U^2 \ , \tag{1}$$

where m_l is the rockslide mass, δm_l is the added mass, U represents the center-of-mass speed, ρ_w is the water density, V_w is the volume of the rockslide in the lake, ϕ the angle of incline, μ is the Coulomb friction coefficient, C_d is the pressure drag coefficient, and A is the surface area of the block perpendicular to the direction of motion. Using $m_l = \rho_l V_l$, where V_l is the volume of the rockslide and ρ_l its density, $\delta m_l = C_m \rho_w V_w$, with C_m the added mass coefficient, and dividing through by $\rho_w V_l$, equation (1) can be rewritten

$$\left(\frac{\rho_l}{\rho_w}+C_m\frac{V_w}{V_l}\right)\frac{dU}{dt}=\left(\frac{\rho_l}{\rho_w}-\frac{V_w}{V_l}\right)g(\sin\phi-\mu\cos\phi) -\frac{C_d A}{2V_l}U^2 \ . \tag{2}$$

Setting $\gamma = \rho_l/\rho_w$ and $\lambda = V_w/V_l$, equation (2) becomes

$$(\gamma+\lambda C_m)\frac{dU}{dt}=(\gamma-\lambda)g(\sin\phi-\mu\cos\phi)-\frac{C_d A}{2V_l}U^2 \ . \tag{3}$$

A simple finite difference scheme can be devised for the rockslide velocity model. Setting the time derivative as a forward difference $dU/dt=(U^{l+1}-U^l)/\Delta t$, and linearizing the squared velocity term by $U^2 = U^{l+1}U^l$ for equation (3) we have

$$\frac{U^{l+1}-U^l}{\Delta t}=a-bU^lU^{l+1} \ ,$$

where

$$a=\frac{\gamma-\lambda}{(\gamma+\lambda C_m)}g(\sin\phi-\mu\cos\phi)$$

and

$$b=\frac{C_d A}{2V_l(\gamma+\lambda C_m)} \ .$$

Rearranging, we obtain an equation giving the speed at time step $l + 1$ in terms of the speed at the previous time step l and known coefficients

$$U^{l+1} = \frac{a\Delta t + U^l}{b\Delta t U^l + 1}. \quad (4)$$

3.2. Tsunami Model

3.2.1. Nonlinear SWE

The numerical model describing the Lake Askja tsunami was set up using GeoClaw [*Berger et al*., 2011], which is a part of the Clawpack package [*LeVeque*, 2002], a collection of numerical methods to solve hyperbolic partial differential equations describing, e.g., wave motion. GeoClaw is an extension to Clawpack where the solution methods from Clawpack are adapted to solving the shallow water equations, which describe flow where the water depth is small in comparison with the lateral length scale.

To solve the shallow water equations, GeoClaw uses high-resolution Godunov-type methods that solve a Riemann problem at each interface between grid cells. These methods have an advantage in that they allow for discontinuous solutions, e.g., shock waves, which often arise in flow problems. The topography is dealt with using a variant of the f-wave scheme, in which topography source terms are incorporated directly into the Riemann problem. Furthermore, the Riemann solver is designed to deal robustly with dry states, both wetting of dry cells as well as the drying of wet cells. For details on the solution algorithms, see *LeVeque* [2002] and *Berger et al*. [2011].

3.2.2. Dispersive Boussinesq Model

The employed dispersive tsunami model is based on a modified set of the Boussinesq equations proposed by *Schäffer et al*. [1993] and *Schäffer and Madsen* [1995]. We coin this model BoussClaw. BoussClaw contains the dispersion terms only in the momentum equations, which simplifies the numerical implementation while maintaining the dispersion relation for waves of shorter wavelengths. Moreover, the equations are written in conservative form. The Boussinesq equations by *Schäffer et al*. [1993] and *Schäffer and Madsen* [1995] can be rearranged with an operator splitting scheme into the shallow water equations part and the dispersion terms. The shallow water equations are first solved using a high-resolution finite volume method and subsequently the dispersion terms are taken into account using a finite difference scheme. In the present application of the model, a wave breaking criterion is chosen based on the ratio of wave height to water depth, η/H. If $\eta/H \geq 0.8$, the set of governing equations is switched to the shallow water equations. A more detailed description of the governing equation and numerical implementation is given in *Kim et al*. [2017].

3.3. Combined Rockslide and Tsunami Model Setup

The rockslide is defined as a block of fixed width with a triangular (wedge-shaped) longitudinal cross section, see Figure 3. Geoclaw reads the time-dependent landslide geometry in gridded form for each time step and adds it on top of the bed topography. To create the files for GeoClaw, the center-of-mass landslide speed profile is calculated by the model described in section 3.1 given a set of values of the parameters describing the rockslide. The part of the landslide that was deposited on land (roughly half of the volume) is neglected and the part which entered the lake is modeled as a wedge-shaped block starting with an initial speed U_0 with the front at the lake level. The subaerial motion is therefore simplified, but as a great part

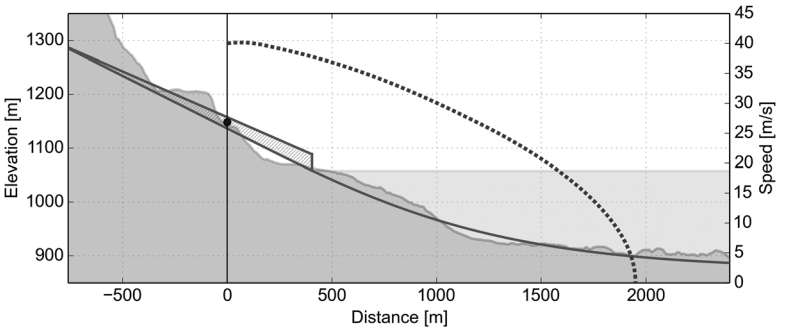

Figure 3. Example center-of-mass speed profile for a rockslide of volume 10×10^6 m^3, width 550 m, initial thickness 30 m, and initial speed 40 m/s. The drag coefficient is set to 1.0 and the added mass coefficient to 1.0. The Coulomb friction coefficient is set at 0.18 which leads to an underwater runout of 1950 m. The speed profile is shown with a thick dotted line along with a cross section of the measured bathymetry, a simplified slope used in the calculation of the CM speed, and a profile of the model rockslide.

of the landslide volume was deposited at the base of the rotational failure plane about 500 m from the lake water level, we believe the simplification not to be too severe. The deposit can be seen clearly in the hillside profile in Figure 3 as a plateau. While the slide it partially submerged, λ in equation (3) grows from 0 to 1. In the speed profile calculation, the wedge-shaped landslide travels down a simplified slope, not the actual terrain, as shown in Figure 3. The local incline is calculated at the location of the CM.

Most of the rockslide parameters are determined from the available field data and the description of the event. The width (550 m) and runout distance (approximately 1950 m) of the rockslide is reasonably well determined from the high-resolution bathymetry. Therefore, for each set of parameter values, the Coulomb friction (μ) was adjusted so that the horizontal runout of the rockslide in the lake was 1950 m. The value varies between 0.15 and 0.2 for the majority of rockslide configurations. The rockslide density is unknown and a value of $\rho_l = 2000$ kg/m^3 is used in all simulations. Values for the added mass C_m and the form drag C_d were both set to unity. We acknowledge, however, that both of these parameters are subject to uncertainty. For a further discussion related to these parameters we refer to *Watts* [1998]. Finally, the shape of the deposits revealed by the multibeam survey shows that the slide path was restricted to a direction of 300–310°N.

The remaining parameters needed to constrain the landslide model are the thickness and speed of the slide as it hit the shoreline. These cannot easily be determined by the field data and therefore an optimization procedure was applied to obtain the most likely values of these, as described in the next subsection. Rough estimates can, however, be made to guide the optimization. The distance from where the rotational failure plane ends to the shoreline is about 600 m and the detailed DEM shows that the slide entered the lake with a width around 550 m. To fit the rockslide into this area, it would have been about 30 m thick when it crossed the shoreline. The impact speed is difficult to estimate due to the uncertainty inherent in the frictional parameters. Assuming only Coulomb friction and gravitational acceleration leads to impact speeds ranging from 20 to 50 m/s for a value of the friction coefficient ranging from $\mu = 0.15$ to 0.3.

Figure 3 shows an example velocity profile for the rockslide block model for the parameter values described above and a simplified bathymetry profile.

3.4. Slide Parameter Sensitivity and Optimization

Due to the uncertainty inherent in the parameters describing the rockslide dynamics, an inverse modeling approach was adopted to determine optimal parameters that best describe the runup of the tsunami. For the NLSW model, the best fit parameters were determined by a grid search whereby the model was run repeatedly for different combinations of parameters. For the Boussinesq model, a global optimization algorithm was employed. A set of initial simulations were carried out to obtain a rough idea of likely rockslide parameter ranges. Three parameters were varied: the angle of impact θ, the impact speed U_0, and the rockslide thickness at impact d. From these simulations, it became clear that varying the angle in the range of 300°–310° (approximately NW) had limited effect on the goodness of fit. Therefore, in the following, only the impact speed and slide thickness were included in the optimization and the angle of impact fixed at 303°. The quality of fit (objective function) was estimated by the sum of squares of the error (*SE*), i.e., summing the squared differences between measured and calculated inundation elevation at regularly spaced points around the lake

$$SE = \sum_{i=1}^{N} \left(h_i^{(meas)} - h_i^{(calc)} \right)^2 .$$

An initial grid search approach revealed that the structure of the sum of squares of the error (*SE*, see above) in parameter space is complex and some testing with gradient-based minimization procedures, such as the Levenberg-Marquardt algorithm, was unsuccessful as such procedures tended to get stuck in local minima. Therefore, a global optimization algorithm was employed to scan the parameter space. The *Differential Evolution* (DE) algorithm [*Storn and Price*, 1997] was chosen and the implementation from the scipy.optimize package used. DE is a relatively simple scheme which utilizes few control variables to guide the minimization. Based on a series of tests, it has been proven to have good convergence properties in comparison with other minimization algorithms. It is a Stochastic direct search method, starting from a random generation of parameter vectors, new trial vectors are formed by perturbing a target vector from the existing

population. The tsunami model is run with the trial vector of parameters and if the resulting objective function is lowered the trial vector replaces the target vector.

4. Results

4.1. NLSW Model Results

Using the GeoClaw NLSW model, the Askja landslide was simulated for a range of values of each parameter to obtain rough bounds on the values which best describe the measured inundation. The parameters that were varied were the impact speed U_0 in the range 15–45 m/s and the rockslide thickness at impact d in the range 20–45 m. Other parameters were kept fixed at $w = 550$ m, $\theta = 303°$, $C_m = 1.0$, $C_d = 1.0$, $\rho_l = 2000$ kg/m^3, and $V_l = 10 \times 10^6$ m^3. The measured and model-calculated maximum inundation for all parameter sets is shown in Figure 4 as a function of angle with respect to the center of the lake, with 0° starting from the east coast and going in a counterclockwise direction. For most of the shoreline, the model parameters can be adjusted to capture the inundation reasonably well. However, this is not the case for the northern shore where the calculated inundation is in most cases significantly higher than the measurements, on average by a factor of 2. Only parameter sets with a low velocity (15–25 m/s) lead to inundation that is close to the measurements along the northern shore, yet typically 5–10 m above measured inundation. For the few parameter sets where the inundation along the north coast is closer to the measurements, the fit worsens elsewhere along the shore, especially close to the point of impact.

4.2. Boussinesq Model Results

The Boussinesq model discussed in section 3.2.2 was applied to investigate whether the discrepancy between the measured and NLSW model-calculated inundation along the northern shore of Lake Askja can be attributed to dispersion.

A grid refinement test was initially carried out to determine a reasonable resolution in terms of accuracy and computational efficiency for the Boussinesq model. The model was run for fixed grid spacings of 12, 20, and 40 m and the wave heights at a number of gauges compared. Running the simulations on finer grid resolutions produced instabilities. The relative difference in height of the first peak between the 20 and 40 m grids compared with runs with a 12 m grid was typically between 5 and 12%, smallest for offshore gauges, increasing toward the shoreline. For the runup height, the relative error for the 20 m grid is 13% compared to the 12 m reference grid. We found this inaccuracy, despite clearly significant, acceptable for the following reasons: The computations in the optimization procedure with a grid spacing below 20 m leads to prohibitively long runs. The fluctuations of the observed runup alongshore is sensitive to the source parameters and we are mostly concerned with hindcasting the overall trends. To this end, the present accuracy was sufficient for us to distinguish the quality of data fit for the Boussinesq model from the NLSW

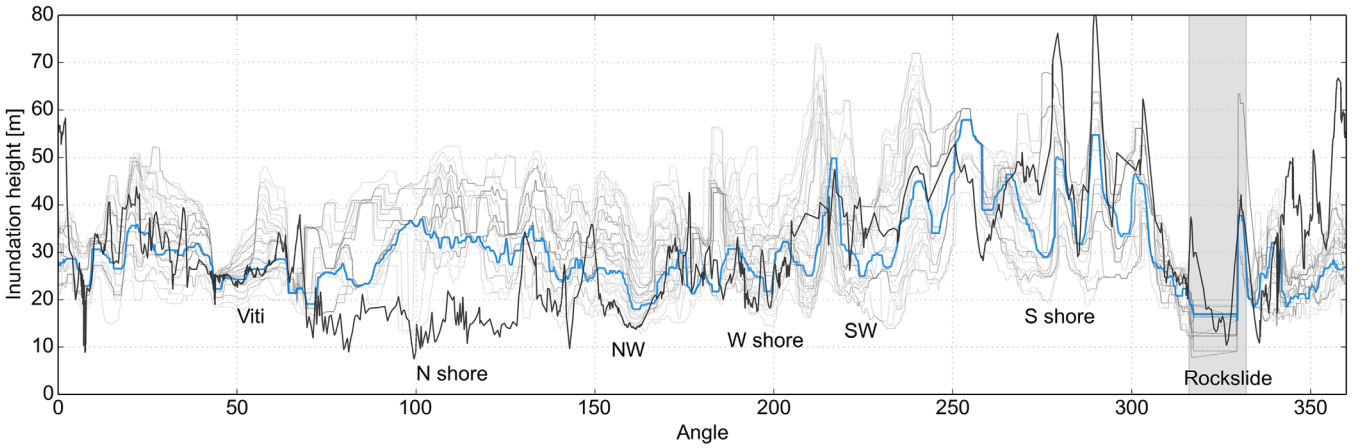

Figure 4. Maximum inundation calculated by the NLSW model for parameter sets $15 \leq U_0 \leq 45$ m/s, $20 \leq d \leq 45$ m, $\theta = 303°$, and $w = 550$ m. The angle is calculated with respect to the center of the lake with 0° starting from the east coast and going in a counterclockwise direction. The results are filtered using a 15-point median filter. Measured inundation is shown with a thick black line and calculated inundation with thin grey lines. Blue line shows the results with the lowest deviation from measured inundation, for landslide parameters $\theta = 303°$, $U_0 = 15$ m/s, and $d = 35$ m.

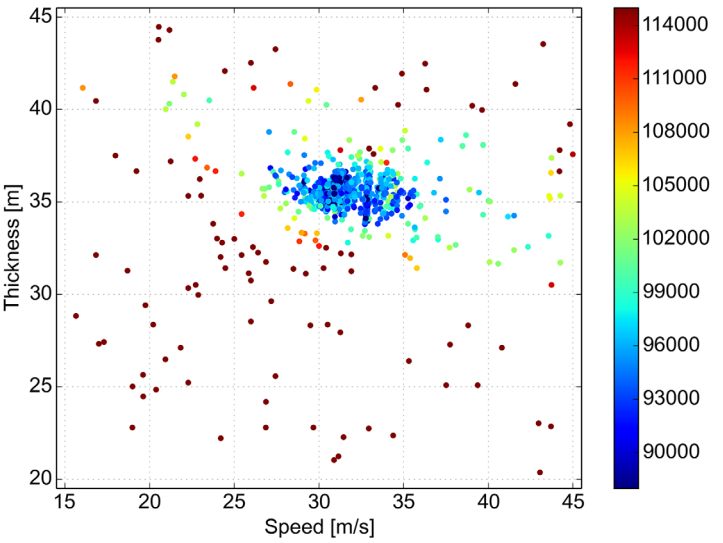

Figure 5. Optimization results for parameter ranges $15 \leq U_0 \leq 45$ m/s, $20 \leq d \leq 45$ m, $w = 550$ m, and $\theta = 303°$. The colored points give the value of the objective function for each model run. Two optimization runs are included in the figure. The maximum calculated objective function was 351.785 and the minimum 80.220, but the color range is clipped to values from 89.000 (dark blue) to 115.000 (dark red) to show the location of the minimum more clearly.

model. Finally, we remark that comparable Boussinesq models are prone to instabilities under demanding conditions where rough topography, large nonlinearities, and fine grids occur together [*Løvholt and Pedersen*, 2009; *Løvholt et al*., 2013]. As a consequence, present Boussinesq models generally cannot operate on very fine grids when subject to large nonlinearities, and the present example is a highly demanding case.

The global optimization procedure using Differential Evolution (see section 3.4) was employed to determine the optimal landslide parameters. For the rockslide speed and thickness, the optimization was run with the bounds $15 \leq U_0 \leq 45$ m/s and $20 \leq d \leq 45$ m. The results are shown in Figure 5. The lowest deviation from measured inundation is obtained for the parameter ranges $30 \leq U_0 \leq 35$ m/s and $34 \leq d \leq 37$ m. The model-calculated maximum inundation for a rockslide model with parameters in the best fitting range, $\theta = 303°$, $U_0 = 30.9$ m/s and $d = 35.5$ m, $w = 550$ m, is shown in Figure 6 along with the measured inundation and the best fitting NLSW model. Overall, the fit is very good and the improvement for the northern shore compared with the NLSW results is notable. More concretely, the objective function for the best fitting NLSW model (160.809) is a factor of 2 higher than that of the Boussinesq model and 97% of the model runs with the dispersive model had a lower objective function than the best fitting NLSW model. We also note that while the solution obtained using the Boussinesq model is following the main runup trend alongshore, the NLSW solution seems to provide a more even distribution. This suggests that the Boussinesq model is the only one being able to capture the radiation pattern due to the rockslide source and the NLSW model is not able to produce the correct inundation pattern even if the rockslide parameters are adapted to fit the observations. To this end, we note that, if the best fit landslide parameters from the Boussinesq model

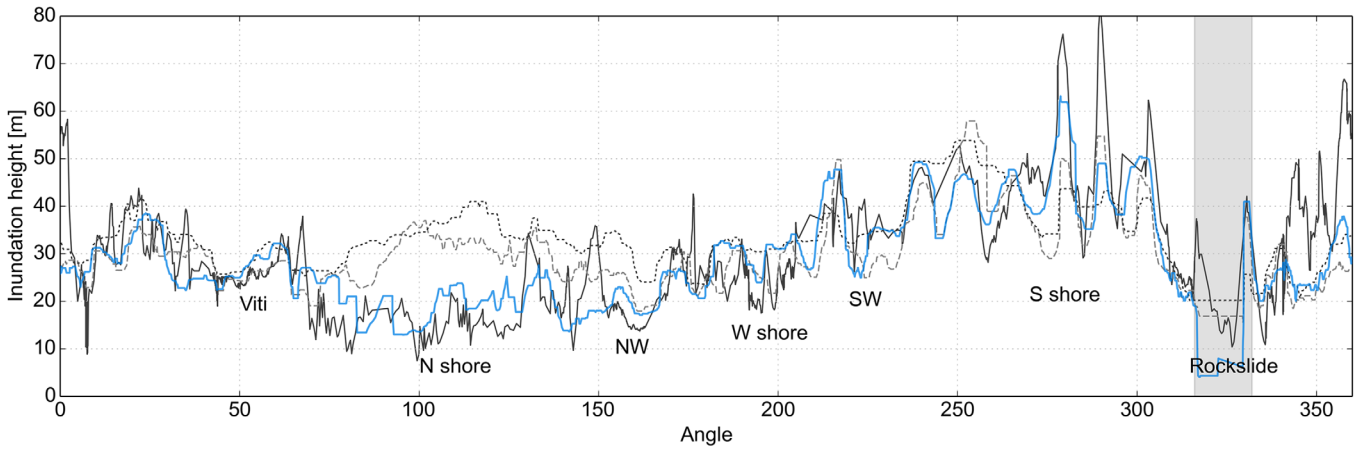

Figure 6. Maximum inundation calculated using the Boussinesq model for the best fitting rockslide model, with $U_0 = 30.9$ m/s, $d = 35.5$ m, $w = 550$ m, and $\theta = 303°$, are shown with a blue line. Measured inundation is shown with a thick black line. A light grey broken line shows the results for the best fitting NLSW model (see Figure 4) and a dark grey dotted line the results of the NLSW model for the best fitting parameters in the Boussinesq model.

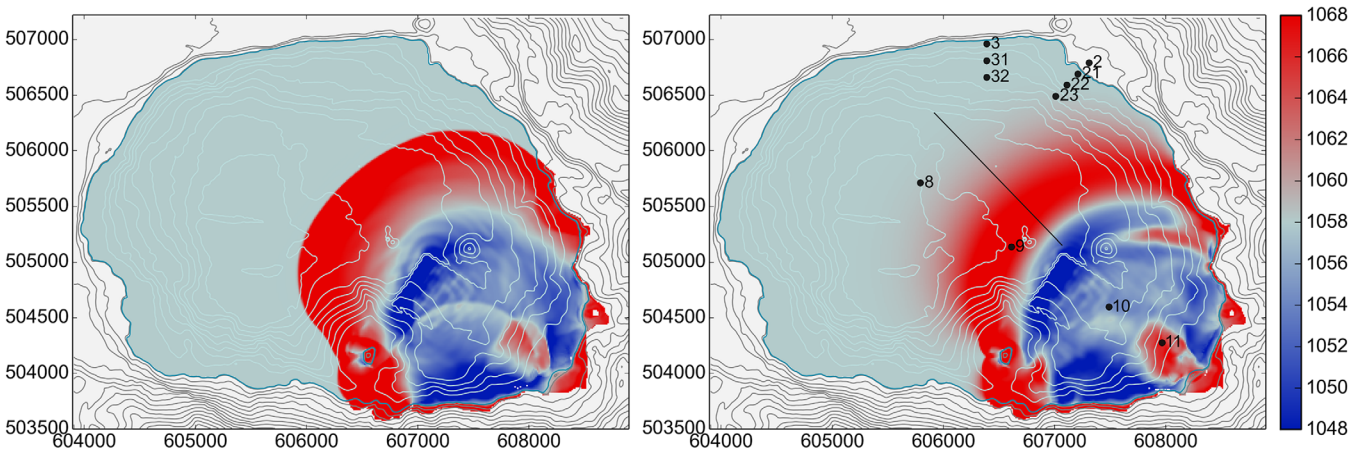

Figure 7. Wavefields at $t = 60$ s for the (left) NLSW and (right) Boussinesq models with rockslide parameters $U_0 = 30.9$ m/s, $d = 35.5$ m, $w = 550$ m, and $\theta = 303°$. Locations of gauges where wave heights are registered during simulations are shown on the right along with a line showing the cross section used in Figure 8. Coordinates on x and y axes are Easting and Northing, respectively, in the ISN93 geodetic reference system.

are used as input to the NLSW model, the NLSW model provides severe offsets compared to the observations (see Figure 6).

Along the southern and southeastern shore, close to the point of impact, the Boussinesq model does not fully capture the extreme peaks of the measured inundation found in narrow gullies. Yet in most cases, the peaks appear in the model results but are not as pronounced as the measured inundation. Also, it must be kept in mind that the uncertainty in the measured data is greatest in this region.

The main reason why the NLSW model cannot capture the inundation pattern on the northern shore becomes clear upon examination of the form of the first wave crest in the two models. The water surface at time $t = 60$ s after impact is shown in Figure 7 for both the NLSW and Boussinesq models. As expected, the frontal wave crest in the NLSW model is very sharp and reflections off the coastline near to the impact site are clearly defined. The wavefield in the Boussinesq model is more diffuse due to frequency dispersion. This is also clear from the transect in Figure 8 where the shape of the leading wave for both models is shown. In the Boussinesq model, frequency dispersion acts to spread out and reduce the wave height of the first crest.

The variations in water level off the northern (gauge 3) and Víti (gauge 21) shores are shown in Figure 9. At gauge 3, the first wave is large and followed by a train of smaller amplitude waves. The maximum inundation on the northern shore is therefore caused by the leading wave, which has a significantly higher amplitude in the NLSW model compared to the Boussinesq model. In contrast to this, the situation at the Víti shore, illustrated by the water level at gauge 21 in Figure 9, is typical of most of the shoreline where the

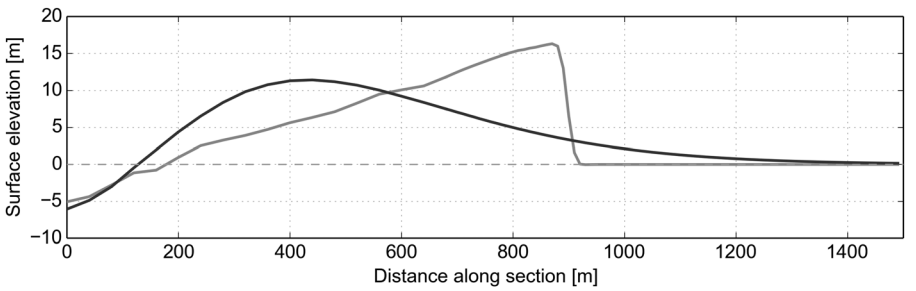

Figure 8. The leading wave for NLSW (light grey) and Boussinesq (dark grey) models for a rockslide model with $U_0 = 30.9$ m/s, $d = 35.5$ m, $w = 550$ m, and $\theta = 303°$. The transect is from $t = 60$ s along the line shown in Figure 7. The location of the leading wave is roughly halfway between gauges 9 and 32 (see Figure 7).

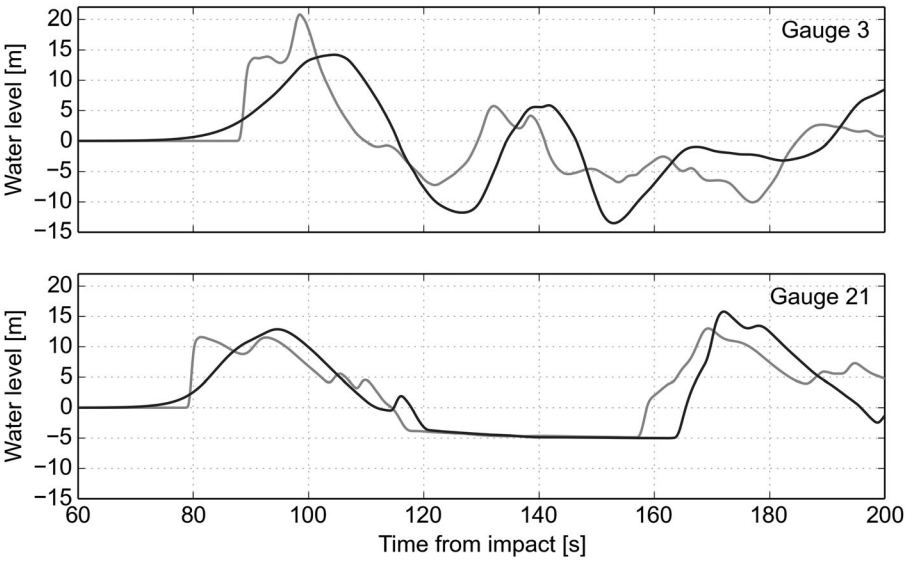

Figure 9. Variations in water level at gauges 21 and 3 for NLSW (light grey) and Boussinesq (dark grey) models for a rockslide model with $U_0 = 30.9$ m/s, $d = 35.5$ m, $w = 550$ m, and $\theta = 303°$. See Figure 7 for gauge locations.

maximum inundation is caused by later arrivals thus masking the effects of dispersion on the amplitude of the leading wave.

Figure 10 shows the evolution of the surface elevation at three different points near the point of impact. At the closest point (gauge 11), the NLSW and Boussinesq surface elevations are at first more or less identical. Further afield (gauge 10), the NLSW and Boussinesq solutions begin to differ, with the NLSW wave being

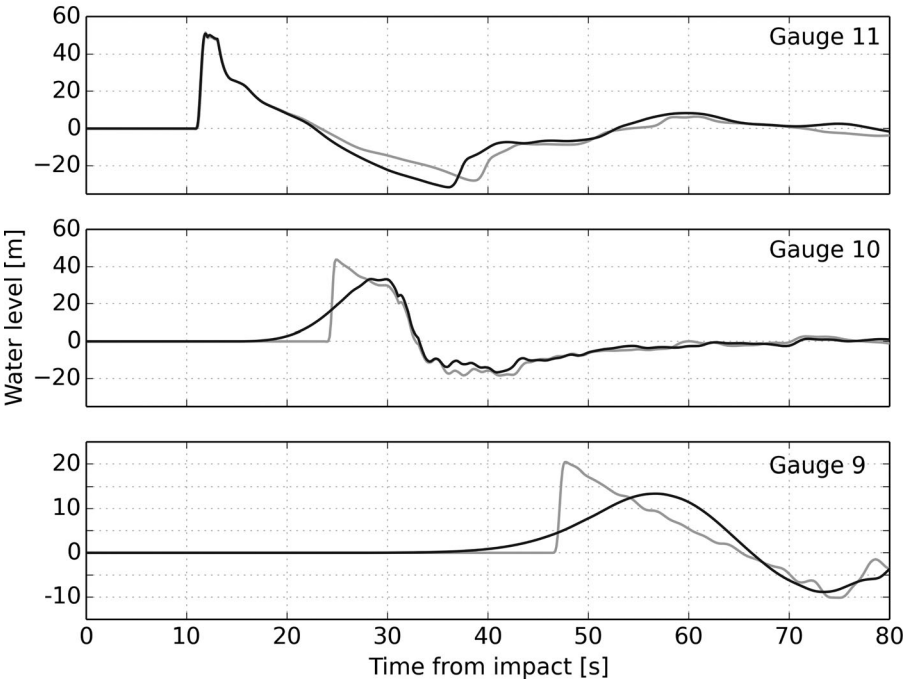

Figure 10. Variations in water level at gauges 9, 10, and 11 for a rockslide model with $U_0 = 30.9$ m/s, $d = 35.5$ m, $w = 550$ m, and $\theta = 303°$ for the NLSW (light grey) and Boussinesq (dark grey) models.

shorter and slightly higher. Close to the basin center (gauge 9), a striking difference between the two models is evident, the NLSW model overestimates the wave height by a factor of 1.4. The difference can be attributed to frequency dispersion, as the main wave generation does not take place between gauges 9 and 10. This is further demonstrated by an estimate of the dispersion time [*Glimsdal et al*., 2013]

$$\tau = \frac{6ht}{gT^3},$$

where h is the water depth, t is the propagation time, g is the gravitational acceleration, and T is a measure of the initial wave period. Based on a number of examples, *Glimsdal et al*. [2013] found that dispersive effects become significant for $\tau > 0.1$. First, we assume that most of the wave generations have taken place at gauge 11, and that τ measures the dispersion from this point on. From Figure 10, we estimate the initial wave period for the pronounced leading peak of the wave system to be roughly 10 s (i.e., double the width of the peak in the NLSW model). A typical water depth between gauge 11 and 10 is $h = 100$ m, and the wave propagation time for the front is 13 s, which gives us $\tau = 0.79$ for the propagation to gauge 10, which indicates a strong effect of dispersion. The long periodic tail is not subject to strong dispersion.

5. Conclusions

A large rockslide was released from the southeast margin of the inner Askja caldera into Lake Askja in the highlands of Iceland on 21 July 2014. Upon entering the lake it caused a large tsunami that traveled across the lake in 1–2 min and inundated the shores around the entire lake with vertical runup measuring up to 60–80 m. Following the event, comprehensive field data were collected, including GPS measurements of the inundation around the lake and multibeam echo soundings of the entire lake bathymetry. This exhaustive data set along with a new Boussinesq-type tsunami model provided a unique opportunity to calibrate a numerical model of the event to explore the effects of dispersion on the wave generation and propagation of landslide-induced tsunamis.

The effect of frequency dispersion for landslide-induced tsunamis has long been acknowledged. The spatial and temporal scales governing the importance of dispersion for tsunamis was systematically studied by *Glimsdal et al*. [2013], and analyzed in particular for submarine landslides by *Løvholt et al*. [2015a]. Dispersion is known to be important for tsunamis originating from rockslides in fjords [*Harbitz et al*., 2014; *Løvholt et al*., 2015b]. Furthermore, *Løvholt et al*. [2008] demonstrated that the radiation pattern from dispersive waves may be expected to be fundamentally different from shallow water waves. However, the present well-documented example has enabled us to show for the first time, combining information from field data with numerical models, that the dispersive model gives a clearly different tsunami wave radiation pattern compared to a shallow water model. As a consequence, we conclude that dispersive effects are crucial in reproducing the observed runup of the Lake Askja tsunami, and that a shallow water model leads to large artificial offsets. Moreover, the study of the event is important because this dispersive nature most likely will occur for other subaerial impact tsunamis as well. The reason for this difference is primarily related to the leading wavefront in the two models. When dispersion is not taken into account, the leading wave has a much higher amplitude than when dispersion acts to spread out the wave energy. For the northern shore of Lake Askja, the first wavefront causes the maximum inundation making its form in the model crucial to obtain a close fit to the measured data. Elsewhere along the shoreline, reflections and edge waves may interfere and increase runup of the subsequent waves.

A limitation in our study is that we do not take into account landslide deformation. Landslide deformation, particularly during impact, will most likely provide a less unidirectional wave than the block.

The global optimization algorithm *Differential Evolution* (DE) proved to be a successful method to determine the rockslide parameters used in the model while local gradient-based minimization was unsuccessful at locating a parameter set with the minimum deviation from measured inundation. The great number of objective function evaluations necessary to locate the minimum with the DE algorithm made it necessary to fix the grid cell size to 20 m, which leads to a limitation on the accuracy of the obtained parameter values

for the Boussinesq model. Still, the impact speed U_0 was constrained to an interval of 5 m/s and the thickness d to 4 m, which considering simplifications made in the modeling of rockslide motion, must be considered an acceptable accuracy.

Acknowledgments

This study was partly done during the first author's research stay at the Norwegian Geotechnical Institute (NGI) in Oslo. S.S.G. thanks NGI for hospitality during the 2 monthlong visits to Oslo. The authors gratefully acknowledge the Nordic Centre of Excellence on Resilience and Societal Security (NORDRESS) for funding the research stay through their mobility grant, as well as providing partial financial support for conducting the research. Part of this work has been supported by the Research Council of Norway under project 231252 (tsunamis induced by large landslides). Additional support for this research was provided by the Icelandic Avalanche and Landslide Fund and the Vatnajökull National Park. Measurements obtained through collaboration with researchers at the Institute of Geography at the University of Innsbruck (UIBK) and the Ludwig-Maximilians-Universität München (courtesy of the IsViews project) are also gratefully acknowledged. The determination of maximum inundation and change in water level was greatly aided by photographs provided by visitors to the area, the participation of the helicopter team of the Icelandic Coast Guard as well as members of the surveying team. Finally, we thank the reviewers for their helpful comments and suggestions. All the data in this manuscript are accessible and can be obtained by e-mail to siggasif@vedur.is.

References

Berger, M. J., D. L. George, R. J. LeVeque, and K. T. Mandli (2011), The GeoClaw software for depth-averaged flows with adaptive refinement, *Adv. Water Res.*, *34*, 1195–1206.

Freundt, A., W. Strauch, S. Kutterolf, and H.-U. Schmincke (2007), Volcanogenic tsunamis in lakes: Examples from Nicaragua and general implications, in *Tsunami and Its Hazards in the Indian and Pacific Oceans*, pp. 527–545, Birkhäuser, Basel, Switzerland.

Fridriksson, A. (2014), What is below the water masses? Multibeam studies of Öskjuvatn, Thingvallavatn and Kleifarvatn, master's thesis, Univ. of Iceland, Reykjavik, Iceland.

Fritz, H. M., F. Mohammed, and J. Yoo (2009), Lituya Bay landslide impact generated mega-tsunami 50th anniversary, *Pure Appl. Geophys.*, *166*, 153–175.

Furseth, A. (1985), *Dommedagsfjellet - Tafjord 1934* [in Norwegian], Gyldendal Norsk Forlag, Oslo, Norway.

Furseth, A. (2009), *Dommedagsfjellet - Tafjordulykka 75 år etter* [in Norwegian], Det Norske Samlaget, Oslo, Norway.

Ghirotti, M. (2012), The 1963 Vaiont landslide, Italy, in *Landslides: Types, Mechanisms and Modeling*, pp. 359–372, Cambridge Univ. Press, Cambridge, U. K.

Glimsdal, S., G. K. Pedersen, C. B. Harbitz, and F. Løvholt (2013), Dispersion of tsunamis: Does it really matter?, *Nat. Hazards Earth Syst. Sci.*, *13*, 1507–1526.

Harbitz, C., G. Pedersen, and B. Gjevik (1993), Numerical simulations of large water waves due to landslides, *J. Hydraul. Eng.*, *119*(12), 1325–1342.

Harbitz, C., S. Glimsdal, F. Løvholt, V. Kveldsvik, G. Pedersen, and A. Jensen (2014), Rockslide tsunamis in complex fjords: From an unstable rock slope at Åkerneset to tsunami risk in western Norway, *Coastal Eng.*, *88*, 101–122.

Hartley, M., and T. Thordarson (2012), Formation of Öskjuvatn caldera at Askja, North Iceland: Mechanism of caldera collapse and implications for the lateral flow hypothesis, *J. Volcanol. Geotherm. Res.*, *227–228*, 85–101.

Hermanns, R., et al. (2014), Earthquake-triggered subaerial landslides that caused large scale fjord sediment deformation: Combined subaerial and submarine studies of the 2007 Aysén fjord event, Chile, in *Engineering Geology for Society and Territory*, vol. 4, pp. 67–70, Springer, Cham, Switzerland.

Jørstad, F. (1968), Waves generated by landslides in Norwegian fjords and lakes, *Tech. Rep. 79*, Norw. Geotech. Inst., Reykjavik, Iceland.

Kiersch, G. (1964), Vaiont reservoir disaster, *Civ. Eng.*, *34*, 32–39.

Kim, J. (2014), Finite volume methods for tsunamis generated by submarine landslides, PhD thesis, Univ. of Wash., Oslo, Norway.

Kim, J., G. Pedersen, F. Løvholt, and R. LeVeque (2017), A Boussinesq type extension of the GeoClaw model—A study of wave breaking phenomena applying dispersive long wave models, *Coast. Eng.*, *122*, 75–86.

Lawrence, M., N. Roberts, and J. Clague (2013), The 2007 Chehalis Lake landslide, British Columbia: A landslide-generated surge wave (tsunami) with implications for dam safety, paper presented at the Proceedings of the GeoMontreal 2013 Conference, Montreal, Canada.

LeVeque, R. J. (2002), *Finite Volume Methods for Hyperbolic Problems*, Cambridge Univ. Press, Seattle, Wash.

Løvholt, F., and G. Pedersen (2009), Instabilities of Boussinesq models in non-uniform depth, *Int. J. Num. Methods Fluids*, *61*, 606–637.

Løvholt, F., G. Pedersen, and G. Gisler (2008), Oceanic propagation of a potential tsunami from the La Palma Island, *J. Geophys. Res.*, *113*, C09026, doi:10.1029/2007JC004603.

Løvholt, F., P. Lynett, and G. Pedersen (2013), Simulating run-up on steep slopes with operational Boussinesq models; capabilities, spurious effects and instabilities, *Nonlinear Processes Geophys.*, *20*, 379–395.

Løvholt, F., G. Pedersen, C. B. Harbitz, S. Glimsdal, and J. Kim (2015a), On the characteristics of landslide tsunamis, *Philos. Trans. R. Soc. A*, *373*.

Løvholt, F., S. Glimsdal, P. Lynett, and G. Pedersen (2015b), Simulating tsunami propagation in fjords with long-wave models, *Nat. Hazards Earth Syst. Sci.*, *15*, 657–669.

Mader, C., and M. Gittings (2002), Modeling the 1958 Lituya Bay mega-tsunami, ii, *Sci. Tsunami Hazards*, *20*(5), 241–250.

Miller, D. (1960), Giant waves in Lituya Bay, Alaska, *U.S. Geol. Surv. Prof. Pap.*, *354-C*, 51–84.

Müller, L. (1964), The rock slide in the Vaiont Valley, *Rock Mech. Eng. Geol.*, *2*, 148–212.

Müller, L. (1968), New considerations on the Vaiont slide, *Rock Mech. Eng. Geol.*, *6*, 1–91.

Naranjo, J. A., M. Arenas, J. Clavero, and O. Muñoz (2009), Mass movement-induced tsunamis: Main effects during the Patagonian Fjordland seismic crisis in Aisèn (45°25′s), Chile, *Andean Geol.*, *36*, 137–145.

Plafker, G., and V. Eyzaguirre (1979), Rock avalanche and wave at Chungar, Peru, in *Rockslides and Avalanches*, 2, pp. 269–279, Elsevier Sci., Cambridge, U. K.

Rist, S. (1975), Stöðuvötn, *Tech. Rep. OS-ROD-7519*, Orkustofnun, Amsterdam, Netherlands.

Roberts, N. J., R. J. McKillop, M. S. Lawrence, J. F. Psutka, J. J. Clague, M.-A. Brideau, and B. C. Ward (2013), Impacts of the 2007 landslide-generated tsunami in Chehalis Lake, Canada, in *Landslide Science and Practice*, vol. 6, pp. 133–140, Springer, Berlin.

Schäffer, H., and P. Madsen (1995), Further enhancements of Boussinesq-type equations, *Coastal Eng.*, *26*(1), 1–14.

Schäffer, H., P. Madsen, and R. Deigaard (1993), A Boussinesq model for waves breaking in shallow water, *Coastal Eng.*, *20*(3), 185–202.

Sepúlveda, S. A., A. Serey, M. Lara, A. Pavez, and S. Rebolledo (2010), Landslides induced by the April 2007 Aysén Fjord earthquake, Chilean Patagonia, *Landslides*, *7*, 483–492.

Sigmundsson, F., et al. (2014), Deflation and deformation of the Askja caldera complex, Iceland, since 1983: Strain and stress development on caldera boundaries prior to tsunami generating rockslide in 2014 at lake Öskjuvatn, Abstract V51A-4715 presented at 2014 Fall Meeting, AGU, San Fransisco, Calif.

Storn, R., and K. Price (1997), Differential evolution—A simple and efficient heuristic for global optimization over continuous spaces, *J. Global Optimization*, *11*, 341–359.

Wang, J., S. N. Ward, and L. Xiao (2015), Numerical simulation of the 4 December 2007 landslide-generated tsunami in Chehalis Lake, Canada, *Geophys. J. Int.*, *201*, 372–376.

Watts, P. (1998), Wavemaker curves for tsunamis generated by underwater landslides, *J. Waterw. Port Coastal Ocean Eng.*, *124*, 127–137.

Weiss, R., H. Fritz, and K. Wünnemann (2009), Hybrid modeling of the mega-tsunami runup in Lituya Bay after half a century, *Geophys. Res. Lett.*, *36*, L09609, doi:10.1029/2009GL037814.